Multiobjective Vector Modulation for Improved Control of NPC-Based Multi-Source Inverters in Hybrid Traction Systems

Emanuele Fedele, Andrea Cervone, Ivan Spina, Diego Iannuzzi, and Andrea Del Pizzo, *Member, IEEE*

Abstract—The concept of a multi-source inverter (MSI) based on NPC topology was recently introduced for hybrid-electric powertrains to connect several dc sources to the traction load in a single conversion stage without magnetics. This work proposes a new modulation algorithm that integrates the tasks of dc currents and ac voltages control at the level of pulsewidth modulation by means of the space-vector formalism. The proposed algorithm allows the MSI to have full control of the dc input currents and fundamental ac output voltages, and enables a higher number of feasible operating modes, including load power sharing between sources and controlled recharging of one source from the other, both in motion and at standstill. Hence, improved control capability of the load and sources is achieved with respect to the state-of-literature modulation approach. To validate the proposed modulation under different operating conditions, steady-state and dynamic tests are performed on a small-scale traction system fed by a primary dc supply and a battery pack. The results are compared with those of the baseline control approach and show that the proposed technique improves the smoothness and flexibility of the control action and reduces the distortion of currents and voltages while ensuring the same converter efficiency.

Index Terms—Electric traction systems, energy storage systems, multi-source inverter (MSI), pulsewidth modulation.

I. Introduction

TRANSPORT electrification is considered a viable solution to reduce the use of fossil fuels and the consequent emission of greenhouse gases [1]. For this reason, the hybridization or complete electrification of propulsion systems has gained a growing interest in automotive, maritime, rail, and aviation industries although at different rates [2]–[6].

Emanuele Fedele, Ivan Spina, Diego Iannuzzi, and Andrea Del Pizzo are with the Department of Electrical Engineering and Information Technology, Università degli Studi di Napoli Federico II, 80125 Naples, Italy (e-mail: emanuele.fedele@unina.it).

Andrea Cervone is with the Power Electronics Laboratory, École Polytechnique Fédérale de Lausanne, 1015 Lausanne, Switzerland (e-mail: andrea.cervone@epfl.ch).

Alternative primary sources (i.e., hydrogen fuel cells) and energy storage devices (i.e., batteries, supercapacitors, and flywheels) represent major enabling technologies for low-carbon transport systems. Their portability, reliability, energy, and power density are key performance factors [7]. Often, the applications' requirements for energy/power density, lifetime, and costs cannot be met by a single technology. Hybrid energy storage systems (HESSs) are, hence, employed to combine the power output of two or more energy sources and storage elements with complementary characteristics. In most cases, one high-energy source and one high-power source are integrated and controlled by means of proper circuitry [8].

Many topologies have been proposed for the interconnection of two independent power sources to a common load [9]. The direct parallelization of the two sources can be employed in low-voltage and/or cost-sensitive applications [10], whereas it is generally avoided in high-power systems due to its limits in the charge/discharge control of the sources. Improved performance can be achieved by placing one or more power converters between the sources and a common dc bus, giving rise to semiactive and fully active topologies [11], [12].

Power-electronics intensive topologies enable high flexibility in the design and control of the sources but typically result in increased system size, complexity, and costs. Power-dense converters can be obtained by reducing the size of heat sinks, magnetics, and capacitors. In the literature, this issue has been tackled through different approaches. On the one hand, high-efficiency wide bandgap semiconductors and intensive liquid cooling for electric machines are key enablers of high system-level performance [13]–[15]. On the other hand, alternative topologies, such as modular multilevel converters [16]–[18] and partial power-processing converters [19], [20], have been proposed to reduce the current/voltage rating of magnetics and capacitors or to completely avoid them. Multi-source inverters (MSIs[1]) based on NPC topologies have been also introduced to interconnect one ac load and multiple dc sources in a single conversion stage without magnetics.

The MSI was first introduced in [21] for compact integration of an energy storage element on board a dc light rail vehicle.

---

[1]The term MSI covers many types of power converters. However, for sake of brevity, in this work, the acronym MSI is specifically used for a multi-source inverter based on the three-level NPC topology.

However, despite the promising results of preliminary experiments, its concept was not further investigated until the contribution of [22], where its application to power-split powertrains of hybrid-electric vehicles was discussed. Further insight into the converter operation and control was given in [23], and vehicle-level simulations were also carried out to evaluate the reduction in power rating of the main dc/dc converter enabled by the MSI-based architecture. In [24] and [25], a reconfigurable version of the MSI was proposed. It is capable of adding up the voltages of the two sources and supplying the load with a higher total dc voltage. This reconfigurability results in a wider constant-torque region of the motor and lower losses at high speed.

In these first research contributions, the MSI was controlled according to a simple strategy called adapted space-vector modulation (SVM). Depending on the required ac output voltage, this strategy employs either one source at a time to supply to the load or the two sources together connected in antiseries. Despite its simplicity, this control approach suffers from major limitations related to the power management of the dc sources. In fact, the sources are never discharged simultaneously with a controllable share of load power, and the controlled recharge of one source from the other cannot be achieved. To tackle some of these issues, an alternative approach to the MSI control problem was introduced in [26] for an HESS comprising batteries and supercapacitors. According to this approach, called the current-sharing control (CSC), the load is periodically connected to one source at a time. The power split between sources can be controlled by acting on the relative conduction time of each source. The CSC achieves the goal of actively controlling the discharge of the two sources. However, in the case of digital implementation, the control of the dc currents is affected by an inherent quantization, that is, the dc power outputs can only be regulated by discrete steps. Moreover, the CSC cannot achieve the controlled recharge of one source from the other, neither in motion nor at standstill [27]. Hence, additional onboard or off-board power converters are needed to recharge bidirectional storage devices. For this reason, an MSI-based system operated under the CSC lacks some of the functionalities of a standard architecture with one or more dc/dc converters and a common dc bus.

This article presents a novel modulation strategy for the MSI that overcomes the drawbacks of the CSC approach. The proposed strategy integrates the twofold task of ac load control and dc power management at the level of pulsewidth modulation by using a space-vector formalism. For this reason, it has been named multiobjective vector modulation (MOVM). The MOVM enables full control of the dc currents while supplying the load with its required ac voltages. Therefore, many operating modes can be managed by the MSI, including the controlled discharge of both sources and the controlled recharge of one source from the other, either during traction or at standstill. The validity of the proposed method is assessed through experimental tests and numerical analyses. The results testify that the MOVM outperforms the CSC in terms of control versatility and smoothness and current/voltage distortion, without penalizing the converter efficiency. Moreover, thanks to its control flexibility, the MOVM narrows the performance
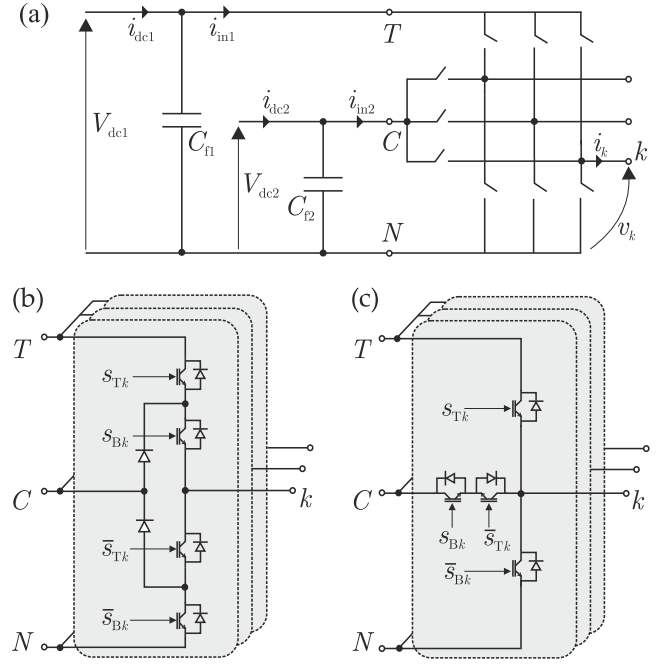

Fig. 1. MSI: (a) ideal topology, (b) NPC implementation, and (c) T-NPC implementation.

gap between MSI-based and standard architectures employing dedicated dc/dc converters. This results in a relevant improvement in the attractiveness of MSIs for traction systems with multiple sources.

The remainder of this article is given as follows. Section II presents the MSI topology and mathematical model and reviews the baseline CSC. In Section III, the proposed modulation algorithm is derived analytically, and its operating domain is discussed. Experimental results are discussed in Section IV, while additional numerical investigations are presented in Section V. Conclusions are drawn in Section VI.

II. MULTI-SOURCE INVERTER

A. Topology

The MSI aims at connecting the ac load to multiple dc sources in a single stage without magnetics for reduced system weight, volume, and overall complexity [22]. Fig. 1 shows the ideal converter topology (a), its neutral point clamped (NPC) (b), and T-NPC (c) circuit implementations in the case of two independent dc inputs. Despite their similarity, the MSI differs from standard multilevel converters because it is supplied by two independent dc sources, which are connected across the terminals $T - N$ and $C - N$, respectively. Their voltage levels V_{dc1} and V_{dc2} are unrelated and appear across the terminals of their respective input capacitors. For NPC and T-NPC circuits, the requirement $V_{dc1} > V_{dc2}$ must be met to avoid short-circuits across the dc inputs. Hence, V_{dc1} and V_{dc2} can be denoted as the high- and low-voltage sources of the MSI, respectively. Each ac output node can be connected to one of the dc terminals through the active switches and clamping diodes according to the switching states listed in Table I, where $k = 1, 2, 3$ refers to the generic converter phase. The four active semiconductor devices of each leg are

TABLE I

SWITCHING STATES OF AN MSI LEG

Output voltage v_k	Switching state	
	s_{Tk}	s_{Bk}
V_{dc1}	1	1
undefined	1	0
V_{dc2}	0	1
0	0	0

divided in two couples that are controlled in a complementary way (i.e., $s_{Tk}/\bar{s}_{Tk}$ and $s_{Bk}/\bar{s}_{Bk}$). The state $\{1, 0\}$ is unfeasible in practice since it makes the output voltage dependent on the direction of the output current (for NPC implementations) or leads to a short-circuit across the high-voltage source (for T-NPC implementations).

B. Mathematical Model

By considering the semiconductor devices as ideal switches, the following equations can be derived through direct inspection of Fig. 1(b) and (c):

$$v_k = s_{Bk} V_{dc2} + s_{Tk}(V_{dc1} - V_{dc2}) \tag{1a}$$

$$i_{in1} = \sum_{k=1}^{3} s_{Tk} i_k \tag{1b}$$

$$i_{in2} = \sum_{k=1}^{3} (s_{Bk} - s_{Tk}) i_k. \tag{1c}$$

To avoid the conduction state $\{1, 0\}$, the switching signals s_{Bk} and s_{Tk} must satisfy the constraint

$$0 \leq s_{Tk} \leq s_{Bk} \leq 1, \qquad k = 1, 2, 3. \tag{2}$$

By introducing the differential switching signal

$$s_{\Delta k} = s_{Bk} - s_{Tk} \tag{3}$$

and averaging (1a)–(1c) over a switching period, the converter averaged model writes as

$$\langle v_k \rangle = d_{Bk} V_{dc1} - d_{\Delta k}(V_{dc1} - V_{dc2}) \tag{4a}$$

$$i_{dc1} = \sum_{k=1}^{3} d_{Tk} \langle i_k \rangle \tag{4b}$$

$$i_{dc2} = \sum_{k=1}^{3} d_{\Delta k} \langle i_k \rangle \tag{4c}$$

where d_{Bk} and $d_{\Delta k}$ are the duty cycles corresponding to the switching signals s_{Bk} and $s_{\Delta k}$, and all the other variables inside angle brackets in (4a)–(4c) refer to the average values of the corresponding variables in (1a)–(1c) over a modulation period. By replacing (3) into (2) and averaging, the following constraint is obtained:

$$0 \leq d_{\Delta k} \leq d_{Bk} \leq 1, \qquad k = 1, 2, 3 \tag{5}$$

which, with a common triangular carrier, automatically ensures (2). It is useful to rewrite the averaged model of the converter by means of the space-vector formalism. For ease of reading, the brackets will be dropped in the following, and all variables

will refer to averaged quantities. By applying the stationary $\alpha\beta$ transform [28] to (4a), the ac output voltage vector $\boldsymbol{v}$ can be expressed as

$$\boldsymbol{v} = v_\alpha + i v_\beta = \boldsymbol{d}_B V_{dc1} - \boldsymbol{d}_\Delta \Delta V \tag{6}$$

where $\boldsymbol{d}_\Delta = d_{\Delta\alpha} + i d_{\Delta\beta}$ and $\boldsymbol{d}_B = d_{B\alpha} + i d_{B\beta}$ are the space vectors of the differential and bottom-switch duty cycles, and $\Delta V = V_{dc1} - V_{dc2}$. Similarly, the central-point dc current can be expressed as

$$i_{dc2} = \frac{3}{2} \, \Re e \left\{ \boldsymbol{d}_\Delta \cdot \check{\boldsymbol{i}} \right\} \tag{7}$$

where $\check{\boldsymbol{i}}$ represents the complex conjugate of the ac currents space vector. Equations (6) and (7) will serve as starting point for the derivation of the proposed modulation.

C. Baseline Current-Sharing Control

The state-of-literature approach to manage the current distribution between two dc sources in an MSI-based architecture consists of operating the MSI as two equivalent two-level VSIs. The MSI periodically connects the ac load to one single dc source at a time, and the relative conduction time of the two sources determines their share of load power. This strategy has been named CSC and presented in [26]. The method defines a current-sharing time period T_{cs} and a corresponding duty cycle d_{cs}, which represents the relative conduction time of V_{dc2} during T_{cs}. The following average-power balance equations result in:

$$p_{dc1} = (1 - d_{cs}) p_{out} \tag{8a}$$

$$p_{dc2} = d_{cs} p_{out} \tag{8b}$$

where p_{dc1}, p_{dc2}, and p_{out} are the average powers of the high-voltage source, low-voltage source, and load, respectively. Therefore, each source can supply from zero to full load power based on the value of d_{cs}.

The operating principle of the CSC is depicted in Fig. 2(a), where, in Mode 1, only V_{dc1} is active, whereas, in Mode 2, only V_{dc2} is active. The operating mode can be obtained by comparing d_{cs} with a sawtooth carrier of period T_{cs} [see Fig. 2(b)]. During each mode, SVM is employed to produce the desired ac voltage by modulating the dc voltage of the active source.

Three main limitations affect this control approach. First, as per its definition, $d_{cs} \in (0, 1)$: the power contribution of each source cannot be greater than the load demand ($>100\%$) or of opposite sign (<0). Consequently, the method cannot achieve the recharge of one source from the other. In fact, a recharge can be obtained by comprising a third operating mode, in which the antiseries of the two sources feed the MSI. However, in this mode, the dc powers are not controlled because the total dc current is set by the load and flows out of one source into the other. For this reason, such a third mode is only mentioned but not further developed in [26].

Second, to keep the MSI in fully controllable operation, both dc input voltages must be equal to or greater than the maximum line-to-line voltage required by the load, irrespective of their actual power output [27].
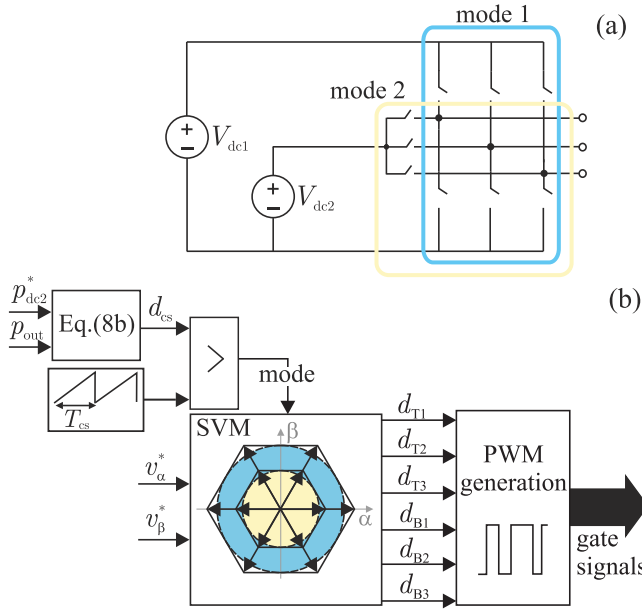
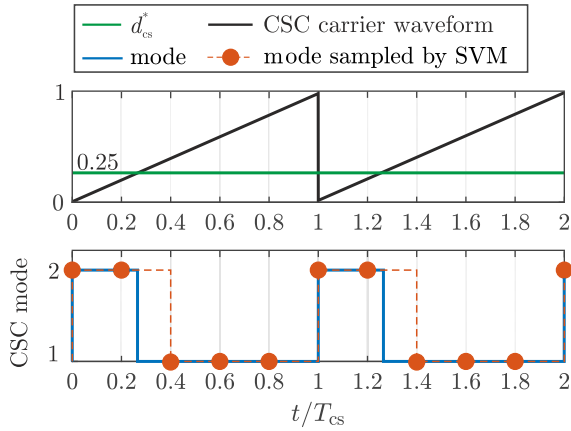Fig. 2. CSC operating principle and implementation: (a) operating modes and (b) control block diagram.

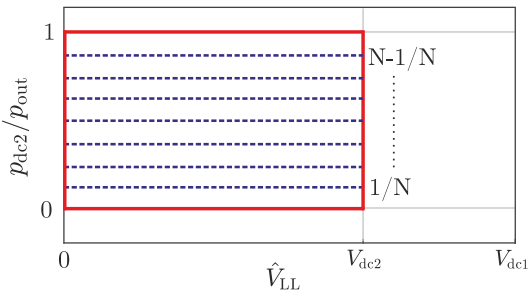Fig. 3. Quantization of the CSC action.

Fig. 4. Operating plane of the CSC algorithm.

Third, the ratio between the current-sharing period T_{cs} and the SVM switching period T_{sw} must of course be integer, i.e., $T_{cs} = NT_{sw}$. This results in an inherent quantization of the current-sharing duty cycle equal to $T_{sw}/T_{cs} = 1/N$. As an example, Fig. 3 shows the case in which $T_{cs}/T_{sw} = 5$. The requested d_{cs} is set to 0.25, but a quantization of 0.2 exists: the MSI ends up working in Mode 2 for two-fifths of the CSC time window, and a wrong duty cycle of 0.4 is actually

obtained. A smaller quantization and better control resolution is achieved with higher values of N, i.e., by enlarging T_{cs}. However, this results in a higher distortion of the MSI input currents, which leads to the increased size of the dc filter capacitors. Therefore, a tradeoff between capacitors' size and control resolution exists.

The drawbacks of the CSC result in the rectangular operating plane shown in Fig. 4, where $\hat{V}_{LL}$ is the peak line-to-line ac voltage and the dotted lines represent the quantized power levels.

III. MULTIOBJECTIVE VECTOR MODULATION

A. Computation of the Duty Cycles

The proposed MOVM overcomes all the limits of the CSC by integrating the twofold task of ac voltage and dc currents control at the level of pulsewidth modulation through a space-vector formalism. The working principle of the MOVM is to derive the six duty cycles d_{Bk} and d_{Tk} based on the ac voltage vector reference $\boldsymbol{v}^*$ and current reference i_{dc2}^* set by the load and dc sources control loops, respectively. The duty cycles are then compared to a common carrier waveform to generate the proper PWM gate signals.

To this aim, (6) and (7) can be arranged into the equation system

$$\begin{cases} d_{B\alpha}V_{dc1} - d_{\Delta\alpha}\Delta V = v_\alpha^* \\ d_{B\beta}V_{dc1} - d_{\Delta\beta}\Delta V = v_\beta^* \\ \dfrac{3}{2}\left(d_{\Delta\alpha}i_\alpha + d_{\Delta\beta}i_\beta\right) = i_{dc2}^* \end{cases} \tag{9}$$

where the $\alpha\beta$ components of the output voltage and current reference are the inputs, and the $\alpha\beta$ components of $\boldsymbol{d}_B$ and $\boldsymbol{d}_\Delta$ are the unknowns. The system (9) has three linear equations in four scalar unknowns and is, thus, underdetermined. Therefore, a degree of freedom exists, and an additional constraint must be formulated. A convenient constraint that simplifies the solution of system (9) is given as follows:

$$\frac{\boldsymbol{d}_\Delta}{|\boldsymbol{d}_\Delta|} = \frac{\boldsymbol{v}^*}{|\boldsymbol{v}^*|}. \tag{10}$$

In fact, it allows to express the reference central-point input current i_{dc2}^* as directly proportional to the load power p_{out} through the vector of differential duty cycles $\boldsymbol{d}_\Delta$

$$i_{dc2}^* = \frac{3}{2}\frac{|\boldsymbol{d}_\Delta|}{|\boldsymbol{v}^*|}\left(v_\alpha^* i_\alpha + v_\beta^* i_\beta\right) = \frac{\boldsymbol{d}_\Delta}{\boldsymbol{v}^*}p_{out}. \tag{11}$$

Ultimately, (9) and (11) are put together to derive a simple and well-posed algebraic system in the $\alpha\beta$ components of the duty cycles, whose solution is

$$\begin{cases} d_{\Delta\alpha} = \dfrac{i_{dc2}^*}{p_{out}}v_\alpha^* \\ d_{\Delta\beta} = \dfrac{i_{dc2}^*}{p_{out}}v_\beta^* \\ d_{B\alpha} = \dfrac{1}{V_{dc1}}\left(v_\alpha^* + \Delta V\dfrac{i_{dc2}^*}{p_{out}}v_\alpha^*\right) \\ d_{B\beta} = \dfrac{1}{V_{dc1}}\left(v_\beta^* + \Delta V\dfrac{i_{dc2}^*}{p_{out}}v_\beta^*\right). \end{cases} \tag{12}$$
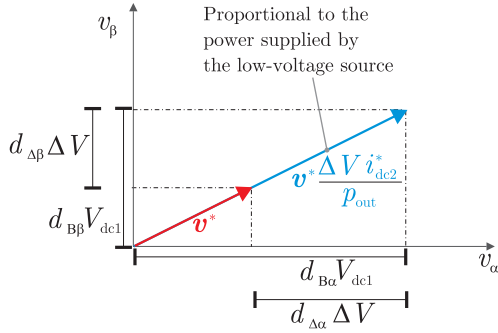
Fig. 5. MOVM space-vector diagram.

Fig. 6. Block diagram of the proposed MOVM.

The above equations constitute the core computation of the proposed vector modulation. They can be interpreted graphically by the space-vector diagram of Fig. 5.

By applying the inverse $\alpha\beta \rightarrow 123$ transform to $\boldsymbol{d}_\Delta$ and $\boldsymbol{d}_B$, the following three-phase sets are obtained:

$$\left[\tilde{d}_{\Delta 1}\ \tilde{d}_{\Delta 2}\ \tilde{d}_{\Delta 3}\right]^T = T_{\alpha\beta \rightarrow 123}\left[d_{\Delta\alpha}\ d_{\Delta\beta}\right]^T \quad (13a)$$

$$\left[\tilde{d}_{B1}\ \tilde{d}_{B2}\ \tilde{d}_{B3}\right]^T = T_{\alpha\beta \rightarrow 123}\left[d_{B\alpha}\ d_{B\beta}\right]^T. \quad (13b)$$

As known from the theory of $\alpha\beta$ transform [28], each of these sets sums up to zero (i.e., it is a "pure" three-phase set) and, thus, comprises at least one negative element. Hence, the quantities obtained through (13a) and (13b) do not comply with the leftmost inequality in (5). Similarly, the rightmost inequality in (5) is not guaranteed in general by the inverse transform and must be imposed separately. Therefore, the sets of duty cycles obtained from (13a) and (13b) cannot be straightly employed to generate the PWM gate signals. The proper bottom and differential duty cycles that comply with (5) are obtained by adding to the pure three-phase sets the following zero-sequence terms:

$$d_{\Delta k} = \tilde{d}_{\Delta k} + z_\Delta, \qquad k = 1, 2, 3 \quad (14a)$$

$$d_{Bk} = \tilde{d}_{Bk} + z_B, \qquad k = 1, 2, 3 \quad (14b)$$

where

$$z_\Delta = -\min\{\tilde{d}_{\Delta 1}, \tilde{d}_{\Delta 2}, \tilde{d}_{\Delta 3}\} \quad (15a)$$

$$z_B = -\min\{\tilde{d}_{B1} - d_{\Delta 1}, \tilde{d}_{B2} - d_{\Delta 2}, \tilde{d}_{B3} - d_{\Delta 3}\}. \quad (15b)$$

Indeed, (14a) shifts the three differential duty cycles $d_{\Delta k}$ above the zero, ensuring the leftmost inequality in (5) and a safe operation of the converter. On the other hand, (14b) shifts each bottom duty cycle d_{Bk} above the differential duty cycle $d_{\Delta k}$ of the same leg, ensuring the middle inequality in (5). Ultimately, the proper duty cycles d_{Tk} for the top components can be obtained from (3). The block diagram of the multiobjective modulation algorithm is shown in Fig. 6.

B. Operating Modes and Linear Modulation Limits

The rightmost inequality in (5) defines the boundary of linear modulation, whose limit occurs when the peak value of the bottom duty cycles d_{Bk} reaches the unit value. For sta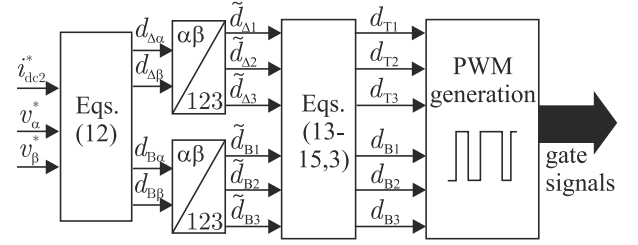ndard PWM techniques of two-level inverters with zero-sequence signal injection, the linear modulation limit occurs when the fundamental line-to-line output voltage has a peak value $\hat{V}_{LL}$ equal to V_{dc} [29]. For the MOVM, the duty cycle magnitudes depend simultaneously on the output voltage, output power, and low-voltage source current as clear from (12). Hence, the limit of linear modulation may be reached depending on the joint values of these quantities. Specifically, the linear modulation region is described by the constraint

$$\mathrm{LT}(\hat{V}_{LL}, V_{dc1}) \le \frac{p_{dc2}}{p_{out}} \le \mathrm{UT}(\hat{V}_{LL}, V_{dc1}, V_{dc2}) \quad (16)$$

where lower and upper thresholds (LT and UT) have been introduced. They depend on the fundamental line-to-line peak output voltage and dc input voltages through the relations

$$\mathrm{LT} = \begin{cases} -\dfrac{V_{dc2}}{\hat{V}_{LL}}, & \text{for}\,\hat{V}_{LL} \le \Delta V \\[2mm] \dfrac{\hat{V}_{LL} - V_{dc1}}{\hat{V}_{LL}}, & \text{for}\,\hat{V}_{LL} \ge \Delta V \end{cases} \quad (17a)$$

$$\mathrm{UT} = \begin{cases} \dfrac{V_{dc2}}{\hat{V}_{LL}}, & \text{for } \hat{V}_{LL} \le V_{dc2} \\[2mm] \dfrac{V_{dc1} - \hat{V}_{LL}}{\hat{V}_{LL}} \cdot \dfrac{V_{dc2}}{\Delta V}, & \text{for } \hat{V}_{LL} \ge V_{dc2}. \end{cases} \quad (17b)$$

For a positive output power, UT and LT determine the positive (discharge) and negative (recharge) power limit of the low-voltage source, respectively. The opposite holds for a negative load power (e.g., during regenerative braking).

Fig. 7(a) shows the peak value of the bottom duty cycles d_{Bk} versus the line-to-line ac voltage and per-unit power level of the low-voltage source; Fig. 7(b) shows the corresponding 2-D linear modulation area and its limits. Three different modulation regions can be identified, which, together with the direction of load power, results in the six feasible operating modes of the MSI listed in Table II. The MOVM enables the MSI to control dc, and the ac power flows in every direction and allows for load power sharing between sources and controlled charging of one source from another. Note that the stationary recharge of one source from the other is achievable if, at standstill, the motor is fluxed by dc currents and, thus, absorbs a small but nonnull amount of power. From a comparison between Figs. 4 and 7(b), it is evident how MOVM expands the operating area resulting from the CSC. Naturally, some of the modes enabled by MOVM may be unfeasible in a specific application, depending on the type of dc sources (i.e., unidirectional or bidirectional). Note from Fig. 7(b) that the UT curve crosses the unity for $\hat{V}_{LL} = V_{dc2}$,
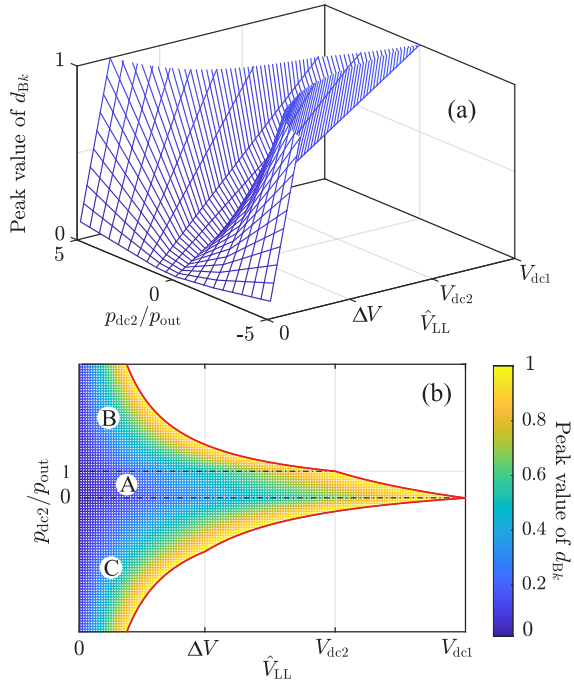
Fig. 7. (a) Peak value of the bottom duty cycles as function of the output voltage $\hat{V}_{LL}$ and per-unit power level of the low-voltage source p_{dc2}/p_{out}. (b) MOVM operating plane and linear modulation limits. Three regions result, corresponding to the MSI operating modes listed in Table II.

TABLE II
MSI OPERATING MODES ENABLED BY THE MOVM

Modulation region	Load operation	
	$p_{out} \geq 0$	$p_{out} < 0$
A	One or both sources supply the load with a controllable share	One or both sources recover the load power with a controllable share
B	V_{dc2} supplies the load and charges V_{dc1} with a controllable current	V_{dc2} recovers all the load power and is also recharged by V_{dc1} with a controllable current
C	V_{dc1} supplies the load and charges V_{dc2} with a controllable current	V_{dc1} recovers all the load power and is also recharged by V_{dc2} with a controllable current

meaning that the low-voltage source cannot process all the load power when its voltage is lower than the required line-to-line output voltage. If such source must potentially supply or recover the entire ac power (e.g., during braking, if V_{dc1} is unidirectional), its voltage must be equal to the maximum load voltage. This also applies to the CSC strategy, which periodically operates the MSI as a two-level VSI fed by one source at a time. This intrinsic feature of an MSI-based architecture can result in a constraint on the selection and sizing of the dc sources, depending on the required system functionalities.

On the other hand, in standard architectures (with dedicated dc/dc converters), p_{dc2} is not limited by the load voltage and can assume any value within the system ratings. This full flexibility is obtained at the cost of one additional power converter and its magnetics. Therefore, the MOVM increases the
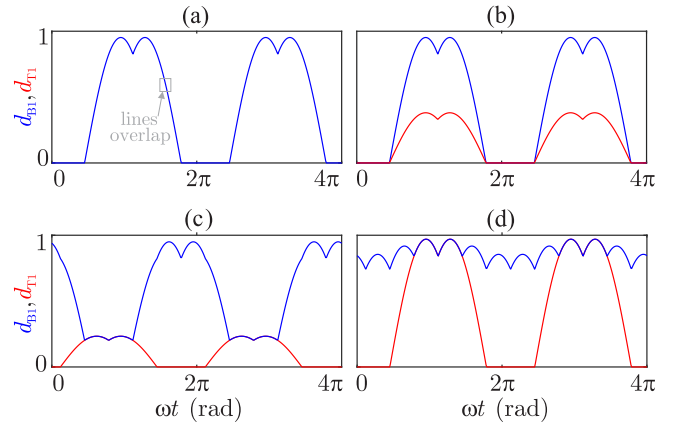

Fig. 8. Duty cycles of the top and bottom switches of the first MSI leg for different setpoints of the low-voltage source output power: (a) $p_{dc2} = 0$, (b) $p_{dc2} = 0.5 \ p_{out}$, (c) $p_{dc2} = 1.5 \ p_{out}$, and (d) $p_{dc2} = -1.5 \ p_{out}$.

control performance and versatility of single-stage MSI-based systems and narrows their gap with standard architectures.

Fig. 8 shows the waveforms of top and bottom duty cycles of the first converter leg in the different modulation regions. The same waveforms apply for the second and third legs with a shift of 120° and 240°, respectively. For every condition, the constraint $d_{Bk} > d_{Tk}$ is always met to ensure a safe operation of the converter. The MOVM results in a downshifted modulation of the top switches [30], with at least one top-duty signal fixed at zero for one-third of the fundamental period. On the other hand, the type of modulation applied to the bottom switches varies with the operating condition. Specifically, when V_{dc2} is inactive [see Fig. 8(a)], d_{Tk} and d_{Bk} overlap, and the MSI is operated as two-level VSI fed by V_{dc1}. When both sources supply the load [modulation region A; see Fig. 8(b)], d_{Bk} and d_{Tk} have the same shape, and their amplitude difference is directly proportional to share of load power supplied by V_{dc2}. When V_{dc1} supplies the load and charges V_{dc2} or vice-versa [regions B and C; see Fig. 8(c) and (d)], the shapes of d_{Bk} differ from the previous conditions so that the desired positive or negative current is imposed in the MSI central terminal.

IV. EXPERIMENTAL RESULTS

A. System Layout

The proposed modulation strategy has been validated and compared to the baseline CSC through experimental tests on a small-scale rail traction system supplied by two separate dc sources. A picture of the test rig is shown in Fig. 9. The circuit comprises a diode rectifier as a high-voltage main power source supplying 350 V, a 250-V battery pack as a low-voltage power supply, an NPC-type MSI, and a 3.5-kW three-phase induction motor. The motor is connected to a small-scale rail wheel set through a transmission chain to simulate a high-inertia load, which is peculiar to traction applications. A standard field-oriented control (FOC) implements the motor speed control, while a closed-loop controller sets the central-point current reference i^*_{dc2} according to the external battery power reference. The proportional–integral (PI) regulators in the
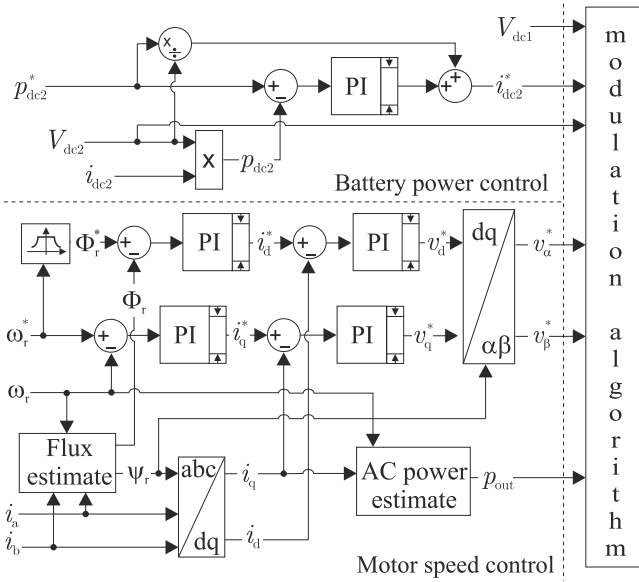
Fig. 9.   Test rig.

Fig. 10.   System control architecture for the experimental tests.

Fig. 11.   Experimental waveforms of ac and dc currents obtained with the MOVM for a steady-state operation of the traction motor: (a) rectifier-only mode, (b) battery-only mode, (c) power sharing between sources, and (d) in-motion recharge of the battery from the rectifier.

control loops are tuned according to well-known standard procedures. To produce proper gate signals, the references of battery current and ac voltages computed by these control loops are processed by the modulation algorithm under test (CSC or MOVM) according to the schemes of Figs. 2(b) or 6, respectively. The overall control architecture is shown in Fig. 10 and has been deployed on a dSpace ds1103 platform operating at a control frequency of 5 kHz. A value of $T_{cs} = 2$ ms was selected for the CSC scheme to obtain a good resolution of 10% with acceptable ripples in the source currents.

B. MOVM Operating Performance Under Steady-State Conditions

Fig. 11 depicts the input and output currents of the MSI controlled through the MOVM strategy for a steady-state operation of the motor and different operating modes of the hybrid traction drive. In particular, Fig. 11(a) and (b) shows the system behavior when the traction power is positive and supplied only by the rectifier or battery, respectively. In both
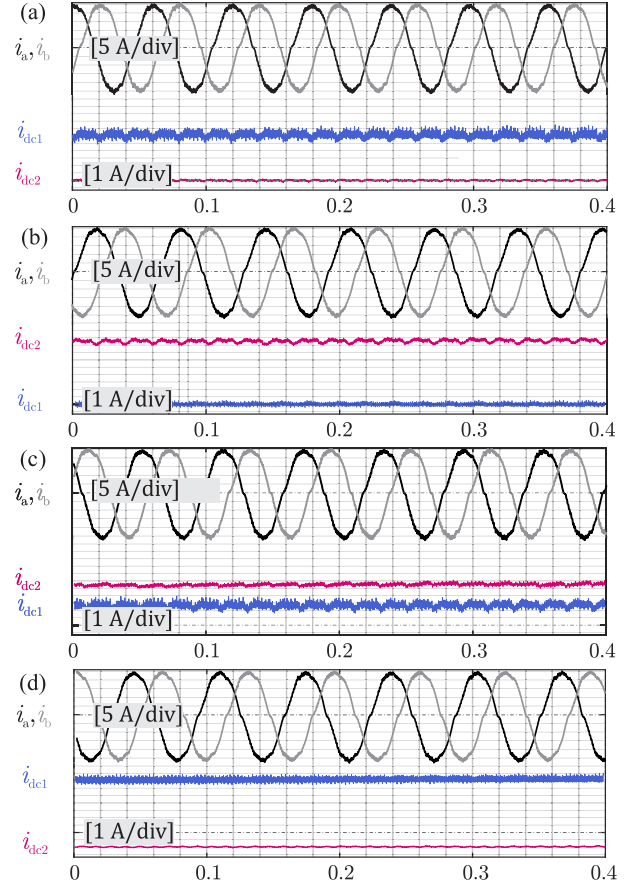
cases, the current of the inactive source is properly kept at zero by the modulation algorithm. In Fig. 11(c), both sources provide power to the motor, whereas the in-motion recharge of the battery from the rectifier is shown in Fig. 11(d). During the recharge, the MSI supplies the motor with its rated currents and sets a negative current in the battery pack. The rectifier output current is higher than in the other operating points since it provides both charging power to the battery and traction power to the motor.

As can be seen, the proposed modulation allows the MSI to control the charge and discharge of the sources while driving the motor with currents being almost sinusoidal, apart from motor nonlinearities. Moreover, the magnitude and harmonic content of the ac currents are not quantitatively affected by the operating mode of the sources. Hence, the dc power management does not interfere with the ac load control, and a decoupling between the two control tasks is achieved by the MOVM algorithm.

C. Performance Comparison Under Dynamic Conditions

The behavior of the proposed modulation has been also evaluated and compared to the baseline CSC approach under a dynamic operation of the traction system. To this aim, the
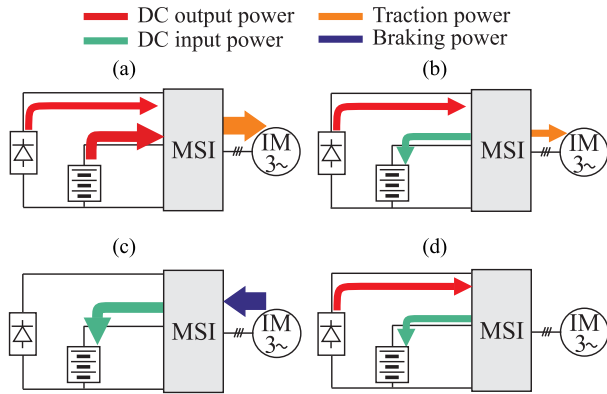
Fig. 12. Operating modes of the traction system during the driving cycle with the corresponding power flows managed by the MSI. (a) Peak shaving. (b) Load leveling. (c) Regenerative braking. (d) Stationary charge.

Fig. 13. System power flows during the driving cycle with the MSI controlled through (a) MOVM and (b) CSC methods.

motor has been operated according to a standard driving cycle comprising acceleration, cruising, and electric braking.

During the driving cycle, the power level of the dc sources was controlled according to the operating modes shown in Fig. 12 and listed in the following.

1) *Peak Shaving:* During the acceleration, the battery pack assists the main power supply and limits its power output to its maximum value of 2.3 kW.
2) *Load Leveling:* During the cruising phase, the battery is recharged at a power level that brings the rectifier output power to its maximum value of 2.3 kW.
3) *Regenerative Braking:* During braking, the battery is controlled to recover the entire amount of braking energy, while the rectifier is inactive.
4) *Stationary Battery Charging:* At standstill, the battery is recharged at 1.5 kW from the rectifier, while the motor is at standstill and develops no torque.

This strategy is representative of typical functionalities of powertrains with multiple sources, e.g., peak shaving at high loads, full regeneration of braking energy, and stationary or dynamic recharge of the storage device from the primary source [31]. It was, therefore, considered appropriate for the scopes of the test.

Fig. 13(a) depicts the system power flows under the MOVM operation. At the beginning of the acceleration, the traction power is below the peak shaving threshold of 2.3 kW, and the MSI properly keeps the battery inactive. As the motor speed and power demand increase, the MOVM achieves a smooth clipping action of the rectifier power output at its limit value as commanded by the EMS. While cruising, the load decreases, and a controlled in-motion recharge of the battery is properly managed by the converter. During braking, full regeneration of the kinetic energy by the battery pack is obtained, while the rectifier is kept inactive. Ultimately, the motor stops and remains at standstill, and the controlled recharge of the battery from the primary supply is properly achieved by the MSI without additional charging circuitry.

From Fig. 13(b), it can be seen that the system behaves differently when the CSC is employed. The peak shaving action during the acceleration is lacking smoothness due to
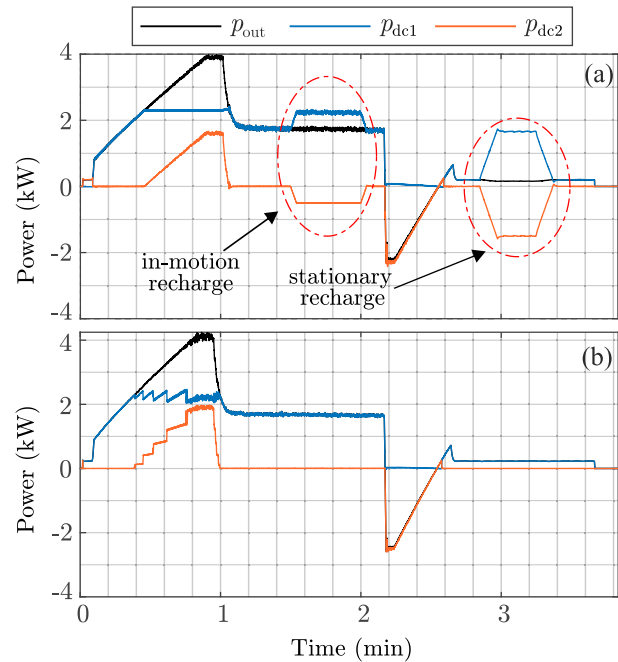
the quantization of the control action, which is an inherent drawback of the CSC approach, while regenerative braking is performed properly. On the other hand, neither in-motion nor stationary controlled recharge of the battery from the primary supply is feasible for the CSC and, thus, could not be performed during the driving cycle. Therefore, an additional power converter would be needed to recharge the storage device and prevent it from overdischarge.

The driving cycle tests validate the proposed modulation in a scenario of dynamic operation. Moreover, they confirm that the MOVM outperforms the CSC in terms of smooth load power sharing between sources and controlled recharging of one source from the other, both with the motor in operation and at standstill.

V. ADDITIONAL NUMERICAL INVESTIGATION

Further simulations with higher time resolution have been carried out to compare MOVM and CSC techniques in terms of ac currents distortion, dc voltage/current ripples, and converter losses. These aspects could not be immediately addressed by inspecting the experimental waveforms due to sampling limitations. The simulations have been performed in Simulink/PLECS environment in the steady-state condition and for several power setpoints. The simulation parameters match those of the experimental setup, while power losses calculation is based on the PLECS thermal model of the 600-V/50-A NPC modules F3L50R06W1E3 by Infineon.

For the first power setpoint of $p_{out} = 4$ kW with a 50% power sharing between sources, the resulting dc voltage and current waveforms are shown in Fig. 14 for both MOVM and CSC methods. It is apparent how MOVM outperforms CSC in terms of current and voltage ripples. This is because

TABLE III
EFFICIENCY, DC RIPPLES, AND AC CURRENT THD FOR MOVM AND CSC METHODS

| p_{dc2} setpoint (kW)	Efficiency (%)		DC currents ripple (A)			DC voltages ripple (mV)			AC current THD (%)	
	MOVM	CSC		MOVM	CSC		MOVM	CSC	MOVM	CSC
2	97.8	97.9	i_{dc1}	0.17	2.51	v_{dc1}	90	1260	0.8	1.0
0.5 pu			i_{dc2}	0.19	3.50	v_{dc2}	100	1730		
0	98.0	98.1	i_{dc1}	0.24	0.27	v_{dc1}	120	130	1.0	1.2
0 pu			i_{dc2}	0	0	v_{dc2}	0	0		
1	97.9	98.1	i_{dc1}	0.22	1.74	v_{dc1}	110	870	0.9	1.1
0.25 pu			i_{dc2}	0.12	2.19	v_{dc2}	70	1110		
3	97.6	97.8	i_{dc1}	0.10	2.09	v_{dc1}	50	1040	0.7	1.0
0.75 pu			i_{dc2}	0.18	3.03	v_{dc2}	90	1520		
4	97.7	97.7	i_{dc1}	0	0	v_{dc1}	0	0	0.6	0.9
1 pu			i_{dc2}	0.20	0.28	v_{dc2}	110	150		
-2	97.1	not supported	i_{dc1}	0.19	not supported	v_{dc1}	90	not supported	0.5	not supported
-0.5 pu			i_{dc2}	0.29		v_{dc2}	140			
6	97.5	not supported	i_{dc1}	0.06	not supported	v_{dc1}	30	not supported	0.5	not supported
1.5 pu			i_{dc2}	0.16		v_{dc2}	90			
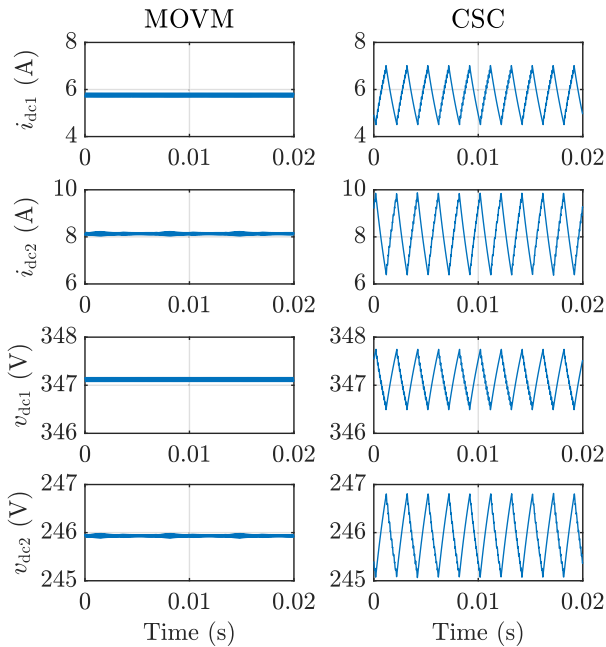
Fig. 14. Comparison between dc current and voltage ripples resulting from MOVM and CSC methods for $p_{out} = 4$ kW and a 50% power sharing between sources.

MOVM operates at the switching frequency $1/T_{sw}$, whereas CSC works at a lower equivalent frequency of $1/T_{cs}$ and, thus, introduces higher distortion in the dc quantities. The specific values of voltage and current ripples in this condition are reported in the first row of Table III, together with the ac current THD and the converter efficiency. The results obtained in the other operating setpoints are also included. Note that some operating points are not supported by the CSC method.

By comparing the dc ripples of MOVM and CSC, it can be noticed that MOVM not only performs better in all considered setpoints but also assures a uniform ripple behavior in the whole p_{dc2} range. Indeed, as explained above, the CSC ripples are significantly higher when the algorithm is actually performing the current sharing. The ripples of the two methods come closer only when p_{dc2} is either 0 or 1 p.u., i.e., when the power sharing is not taking place. Furthermore, MOVM yields better THD values of the load current and comparable efficiencies. Thus, despite not being intended for this purpose, MOVM neither compromises the efficiency nor introduces higher distortions in the system but rather improves its overall performance.

VI. CONCLUSION

This article proposed a new modulation algorithm for NPC-based MSIs used in hybrid powertrains for single-stage integration and control of two dc sources and one ac load without intermediate dc/dc converters. The proposed multiobjective modulation algorithm has been derived from the converter analytical model, and its linear modulation boundaries have been presented and discussed in detail. These boundaries determine the charge/discharge power limits of the dc sources as a function of their voltage level and the magnitude of the ac output voltages. By exploiting its circuit topology, the proposed technique enables the MSI to fully control the dc input currents and ac output voltages. In particular, the controlled recharge of one source from the other can be managed by the MSI both during motion and at standstill, eliminating the need for additional dc/dc converters. This represents a relevant improvement over the state-of-literature CSC approach, which does not exploit the MSI circuit topology and fails to achieve a smooth power sharing and a controlled static or dynamic recharge of one source from another.

Experimental tests have been performed on a small-scale traction system fed by two dc sources to validate the proposed modulation under both steady-state and dynamic operations of the traction motor. The results have confirmed that the

modulation enables the MSI to manage several operating modes, characterized by dc and ac power flows of variable magnitude and direction. In this sense, the proposed technique outperforms the baseline CSC approach, allowing the MSI for smoother and more versatile control of system power flows.

Furthermore, as testified by additional numerical investigations, the improvements brought by MOVM extend also to dc current/voltage ripples and THD of the ac load currents.

In light of these results, the proposed multiobjective modulation algorithm brings a relevant improvement to the performance of MSI-based traction systems. For this reason, it can be seen as a promising solution to unfold the full potential of MSIs and support their adoption in highly integrated powertrains supplied by multiple sources.

REFERENCES

[1] R. Zhang and S. Fujimori, "The role of transport electrification in global climate change mitigation scenarios," *Environ. Res. Lett.*, vol. 15, no. 3, Feb. 2020, Art. no. 034019.

[2] G. Meyer, "Electrification of the transport system—Expert group report," Eur. Commission-Directorate-Gen. Res. Innov., Brussels, Belgium, Tech. Rep., Nov. 2017. [Online]. Available: https://op.europa.eu/en/publication-detail/-/publication/253937e1-fff0-11e7-b8f5-01aa75ed71a1/language-en/format-PDF

[3] R. R. Kumar and K. Alok, "Adoption of electric vehicle: A literature review and prospects for sustainability," *J. Cleaner Prod.*, vol. 253, Apr. 2020, Art. no. 119911.

[4] B. J. Brelje and J. R. R. A. Martins, "Electric, hybrid, and turbo-electric fixed-wing aircraft: A review of concepts, models, and design approaches," *Prog. Aerosp. Sci.*, vol. 104, pp. 1–19, Jan. 2019.

[5] E. Fedele, D. Iannuzzi, and A. D. Pizzo, "Onboard energy storage in rail transport: Review of real applications and techno-economic assessments," *IET Electr. Syst. Transp.*, vol. 11, no. 4, pp. 279–309, Dec. 2021, doi: 10.1049/els2.12026.

[6] S. Fang, Y. Wang, B. Gou, and Y. Xu, "Toward future green maritime transportation: An overview of seaport microgrids and all-electric ships," *IEEE Trans. Veh. Technol.*, vol. 69, no. 1, pp. 207–219, Jan. 2020.

[7] P. Ralon, M. Taylor, A. Ilas, H. Diaz-Bone, and K.-P. Kairies, "Electricity storage and renewables: Costs and markets to 2030," Int. Renew. Energy Agency (IRENA), Abu Dhabi, UAE, Tech. Rep., Oct. 2017. [Online]. Available: https://www.irena.org/-/media/Files/IRENA/Agency/Publication/2017/Oct/IRENA_Electricity_Storage_Costs_2017.pdf

[8] S. Vazquez, S. M. Lukic, E. Galvan, L. G. Franquelo, and J. M. Carrasco, "Energy storage systems for transport and grid applications," *IEEE Trans. Ind. Electron.*, vol. 57, no. 12, pp. 3881–3895, Dec. 2010.

[9] D.-D. Tran, M. Vafaeipour, M. El Baghdadi, R. Barrero, J. Van Mierlo, and O. Hegazy, "Thorough state-of-the-art analysis of electric and hybrid vehicle powertrains: Topologies and integrated energy management strategies," *Renew. Sustain. Energy Rev.*, vol. 119, Mar. 2020, Art. no. 109596.

[10] H. Liu, Z. Wang, J. Cheng, and D. Maly, "Improvement on the cold cranking capacity of commercial vehicle by using supercapacitor and lead-acid battery hybrid," *IEEE Trans. Veh. Technol.*, vol. 58, no. 3, pp. 1097–1105, Mar. 2009.

[11] A. L. Allegre, A. Bouscayrol, and R. Trigui, "Influence of control strategies on battery/supercapacitor hybrid energy storage systems for traction applications," in *Proc. IEEE Vehicle Power Propuls. Conf.*, Sep. 2009, pp. 213–220.

[12] Z. Song, H. Hofmann, J. Li, X. Han, X. Zhang, and M. Ouyang, "A comparison study of different semi-active hybrid energy storage system topologies for electric vehicles," *J. Power Sources*, vol. 274, pp. 400–411, Jan. 2015.

[13] J. Biela, M. Schweizer, S. Waffler, and J. W. Kolar, "SiC versus Si—Evaluation of potentials for performance improvement of inverter and DC–DC converter systems by SiC power semiconductors," *IEEE Trans. Ind. Electron.*, vol. 58, no. 7, pp. 2872–2882, Jul. 2011.

[14] A. Rujas, V. M. López, A. García-Bediaga, A. Berasategi, and T. Nieva, "Influence of SiC technology in a railway traction DC–DC converter design evolution," in *Proc. IEEE Energy Convers. Congr. Expo.*, Nov. 2017, pp. 931–938.

[15] Z. Liang, P. Ning, and F. Wang, "Development of advanced all-SiC power modules," *IEEE Trans. Power Electron.*, vol. 29, no. 5, pp. 2289–2295, May 2014.

[16] M. Hagiwara, K. Nishimura, and H. Akagi, "A medium-voltage motor drive with a modular multilevel PWM inverter," *IEEE Trans. Power Electron.*, vol. 25, no. 7, pp. 1786–1799, Jul. 2010.

[17] C. Gan, Q. Sun, J. Wu, W. Kong, C. Shi, and Y. Hu, "MMC-based SRM drives with decentralized battery energy storage system for hybrid electric vehicles," *IEEE Trans. Power Electron.*, vol. 34, no. 3, pp. 2608–2621, Mar. 2019.

[18] N. Mukherjee and P. Tricoli, "A new state of charge control of modular multilevel converters with supercapacitors for traction drives," in *Proc. IEEE Energy Convers. Congr. Expo.*, Oct. 2015, pp. 3674–3680.

[19] J. Anzola et al., "Review of architectures based on partial power processing for DC–DC applications," *IEEE Access*, vol. 8, pp. 103405–103418, 2020.

[20] J. Rojas, H. Renaudineau, S. Kouro, and S. Rivera, "Partial power DC–DC converter for electric vehicle fast charging stations," in *Proc. 43rd Annu. Conf. IEEE Ind. Electron. Soc. (IECON)*, Dec. 2017, pp. 5274–5279.

[21] M. Chymera, A. C. Renfrew, M. Barnes, and J. Holden, "Simplified power converter for integrated traction energy storage," *IEEE Trans. Veh. Technol.*, vol. 60, no. 4, pp. 1374–1383, May 2011.

[22] L. Dorn-Gomba, P. Magne, B. Danen, and A. Emadi, "On the concept of the multi-source inverter for hybrid electric vehicle powertrains," *IEEE Trans. Power Electron.*, vol. 33, no. 9, pp. 7376–7386, Sep. 2018.

[23] L. Dorn-Gomba, J. Guo, and A. Emadi, "Multi-source inverter for power-split hybrid electric powertrains," *IEEE Trans. Veh. Technol.*, vol. 68, no. 7, pp. 6481–6494, Jul. 2019.

[24] E. Chemali and A. Emadi, "On the concept of a novel reconfigurable multi-source inverter," in *Proc. IEEE Transp. Electrific. Conf. Expo (ITEC)*, Jun. 2017, pp. 707–713.

[25] O. Salari, K. H. Zaad, A. Bakhshai, and P. Jain, "Reconfigurable hybrid energy storage system for an electric vehicle DC-AC inverter," *IEEE Trans. Power Electron.*, vol. 35, no. 12, pp. 12846–12860, Dec. 2020.

[26] L. Dorn-Gomba, E. Chemali, and A. Emadi, "A novel hybrid energy storage system using the multi-source inverter," in *Proc. IEEE Appl. Power Electron. Conf. Expo. (APEC)*, Mar. 2018, pp. 684–691.

[27] E. Fedele, D. Iannuzzi, P. Tricoli, and A. D. Pizzo, "NPC-based multi-source inverters for multimode DC rail traction systems," *IEEE Trans. Transp. Electrific.*, early access, May 13, 2022, doi: 10.1109/TTE.2022.3175097.

[28] S. Chattopadhyay, M. Mitra, and S. Sengupta, "Clarke and park transform," in *Lectric Power Quality*. Berlin, Germany: Springer, 2011, pp. 89–96.

[29] K. Zhou and D. Wang, "Relationship between space-vector modulation and three-phase carrier-based PWM: A comprehensive analysis," *IEEE Trans. Ind. Electron.*, vol. 49, no. 1, pp. 186–196, Feb. 2002.

[30] Y. Huang et al., "Analytical characterization of CM and DM performance of three-phase voltage-source inverters under various PWM patterns," *IEEE Trans. Power Electron.*, vol. 36, no. 4, pp. 4091–4104, Apr. 2021.

[31] G. Abad, *Power Electronics and Electric Drives for Traction Applications*, G. Abad, Ed. Chichester, U.K.: Wiley, 2016.

Emanuele Fedele received the B.Sc. and M.Sc. degrees in electrical engineering from the Department of Electrical Engineering and Information Technology, University of Naples Federico II, Naples, Italy, in 2015 and 2018, respectively, where he is currently pursuing the Ph.D. degree in electrical engineering.

His research interests include modeling and control of power electronics, and electrical drives for traction systems.

Andrea Cervone received the B.Sc., M.Sc., and Ph.D. degrees in electrical engineering from the University of Naples Federico II, Naples, Italy, in 2014, 2017, and 2021, respectively.

He currently holds a post-doctoral position at the École Polytechnique Fédérale de Lausanne (EPFL), Lausanne, Switzerland. His research interests include multilevel converters and multiphase electrical drives. linenumberpar

Diego Iannuzzi was born in Naples, Italy, in 1972. He received the M.Sc. *(cum laude)* and Ph.D. degrees in electrical engineering from the University of Naples Federico II, Naples, Italy, in 1998 and 2001, respectively.

He was a Visiting Professor with the University of South Carolina, Columbia, SC, USA, the École Polytechnique Fédérale de Lausanne (EPFL), Lausanne, Switzerland, the Institut National Polytechnique de Toulouse, Toulouse, France, and the Polytechnic University of Milan, Milan, Italy, where he was involved in the field of electrical drives for traction applications. He has been with the Traction Competence Centre of Campania, Naples, since 2004, where he was involved in research activities. He has been an Associate Professor with the Department of Electrical Engineering, University of Naples Federico II, since 2005.

Ivan Spina was born in Naples, Italy, in 1982. He received the M.S. *(cum laude)* and Ph.D. degrees in electrical engineering from the University of Naples Federico II, Naples, Italy, in 2008 and 2012, respectively.

From 2012 to 2013, he was a Post-Doctoral Research Fellow with the Department of Electrical Engineering, University of Naples Federico II. Since 2014, he has been an Assistant Professor of electrical machines and drives with the Department of Electrical Engineering and Information Technology, University of Naples Federico II. In 2017, he was invited as a Research Fellow by the Birmingham Centre for Railway Research and Education, Birmingham, U.K. In 2018, he joined the Teaching Team, University of Birmingham Programme in Urban Railway Engineering, Singapore. He has authored or coauthored several scientific papers published in international journals and conference proceedings. His research interests include modeling, diagnostic and control of power electronics, and electrical drives for industrial and traction applications.

Andrea Del Pizzo (Member, IEEE) received the M.S. degree in electrical engineering from the University of Naples Federico II, Naples, Italy, in 1979.

He became an Assistant Professor in 1983 and a Full Professor of electrical machines and drives in 2001 at the University of Naples Federico II. He was also a Contract Professor with the University of Cassino, Cassino, Italy, and the University of Sannio, Benevento, Italy. Since 2013, he has been the Head of the Research Center on Electric Propulsion of Land, Sea, and Air Vehicles, University of Naples Federico II. He has been responsible and/or a coordinator of many research projects, including private companies and public research institutions. His main research interests include modeling of electrical machines and drives, high-performance permanent-magnet brushless and induction motor drives, modular multilevel converters, and high-power-density drives for electric propulsion.

Prof. Del Pizzo is also a general co-chairman of an international conference on power electronics and electrical drives.